



# Synchronous role of coupled adsorption and photocatalytic oxidation on ordered mesoporous anatase TiO<sub>2</sub>–SiO<sub>2</sub> nanocomposites generating excellent degradation activity of RhB dye

Weiyang Dong<sup>a,\*</sup>, Chul Wee Lee<sup>b</sup>, Xinchun Lu<sup>c</sup>, Yaojun Sun<sup>c</sup>, Weiming Hua<sup>d</sup>, Guoshun Zhuang<sup>a</sup>, Shicheng Zhang<sup>a</sup>, Jianmin Chen<sup>a</sup>, Huiqi Hou<sup>a</sup>, Dongyuan Zhao<sup>d,\*</sup>

<sup>a</sup> Department of Environmental Science and Engineering, Fudan University, 220 Handan Road, Shanghai 200433, PR China

<sup>b</sup> Advanced Chemical Technology Division, Korea Research Institute of Chemical Technology, P.O. Box 107, Yuseong, Daejeon 305-600, Korea

<sup>c</sup> Center for Analysis and Measurement, Fudan University, 220 Handan Road, Shanghai 200433, PR China

<sup>d</sup> Department of Chemistry, Fudan University, 220 Handan Road, Shanghai 200433, PR China

## ARTICLE INFO

### Article history:

Received 6 November 2009

Received in revised form 12 December 2009

Accepted 17 December 2009

Available online 29 December 2009

### Keywords:

Synchronous role

Adsorption

Photocatalytic oxidation

Ordered mesoporous anatase TiO<sub>2</sub>–SiO<sub>2</sub> nanocomposites

RhB dye

## ABSTRACT

In this paper, we report a synchronous role of coupled adsorption and photocatalytic oxidation on ordered 2-D hexagonal mesoporous TiO<sub>2</sub>–SiO<sub>2</sub> nanocomposites with large pore channels (>4.0 nm) and high specific surface areas (>70 m<sup>2</sup> g<sup>−1</sup>). These mesoporous frameworks consist of anatase TiO<sub>2</sub> nanocrystals and amorphous SiO<sub>2</sub> nanomatrixes, which link mutually, coexist to form unique composite-walls, providing unprecedented spaces for “the synchronous role of coupled adsorption and photocatalytic oxidation”. SiO<sub>2</sub> nanomatrixes are excellent adsorbents, providing better adsorption centers and enriching organic pollutant molecules; while anatase nanocrystals behave as photocatalytic active sites to oxidize the organic molecules pre-enriched by the surrounding SiO<sub>2</sub> particles. Moreover, the high accessible surface areas can provide more adsorptive and photocatalytically active sites; and the large mesopore channels allow the reactive molecules to diffuse more easily both into and out of the inner surfaces before and after photocatalytic reactions, respectively. Our strategy realizes the synchronous role by adjusting Ti/Si ratios, the number of surface hydroxyls, the size and crystallinity of the anatase nanocrystals on the unique composite-frameworks. The cationic rhodamine-B (RhB) dye is used as the target pollutant to characterize the adsorption performance and photocatalytic activities. Our results show that the synchronous role results in excellent photocatalytic degradation activity ( $k = 0.231 \text{ min}^{-1}$ ), which is much higher than that of Degussa commercial P25 photocatalyst ( $k = 0.0671 \text{ min}^{-1}$ ).

© 2009 Elsevier B.V. All rights reserved.

## 1. Introduction

Ubiquitous dyestuffs are one of the most notorious contaminants in aquatic environments because of their huge volume of production from industries, slow biodegradation and decoloration, and toxicity [1–2]. About 700 000 tons of dyes are annually produced in the world [1,3], and more than 15% of which, about 400 tons per day, are released into the environment during manufacturing, processing and using [4–5]. It is well-known that some azo, fluorine dyes, and their degradation products such as aromatic amines are highly carcinogenic and mutagenic [6–7]. Rhodamine B (RhB), a xanthene dye, is widely used as a colorant in textiles and food stuffs, and also a well-known water tracer

fluorescent. RhB is harmful if swallowed by human beings and animals, and causes irritation to the skin, eyes and respiratory tract. The carcinogenicity, reproductive and developmental toxicity, neurotoxicity and chronic toxicity towards humans and animals have been experimentally proven [8].

Conventional methods such as coagulation, flocculation, reverse osmosis *etc.* have been used to deal with wastewaters containing dyes. However, many drawbacks still exist in these methods due to the increasing number of refractory materials in wastewater effluents, difficulties in the complete removal of color and expensiveness [9–10]. Conventional aerobic biological processes also do not treat dye wastewater effectively because of the large degree of aromatics present in the molecules, the stability of modern dyes to light and oxidizing agents, and the inherent reluctance to biodegradation [7,11–12]. Accordingly, the effective removal of dye effluents remains a challenge [12].

In the past decades, many investigations have been extensively conducted for removing dye pollutants worldwide, including

\* Corresponding authors. Tel.: +86 021 55665189; fax: +86 021 65643597.

E-mail addresses: [wuydong@fudan.edu.cn](mailto:wuydong@fudan.edu.cn) (W. Dong), [dyszao@fudan.edu.cn](mailto:dyszao@fudan.edu.cn) (D. Zhao).

activated carbon adsorption [7,10,13], photocatalytic oxidation [1–4,6–9,11–12,14–20], photoelectrocatalytic oxidation [5], coupled photocatalytic oxidation and biofilm process [11], integrated microwave/UV-illuminated method [21], Fenton and photo-Fenton processes [22], etc. Although activated carbon adsorption is an effective means for dyes removal [7,10,13], it is still considered as an expensive method mainly due to the non-renewable use [13]. Among those approaches, photocatalytic oxidations have attracted great attention as emerging successful technologies [23]. Up to now,  $\text{TiO}_2$  heterogeneous photocatalytic technology has been regarded to be the most efficient, environmentally benign and promising method, and numerous researches are focusing on it because of its nontoxicity, high photochemical stabilities, low cost, outstanding oxidative power [23–24]. However, one of the main drawbacks is very poor adsorptive power to some dyes [14,16] and other organic pollutants [25–28]. It is documented that heterogeneous photocatalytic reactions occur at the surface rather than in the solution bulk, and the surface properties of  $\text{TiO}_2$  are critical for the efficiencies [16,18]. Pre-adsorption on the surface of  $\text{TiO}_2$  particles is prerequisite for efficiently photocatalytic degradation of dyes, and greater adsorption enhances the rate [16,21,29]. To pre-enrich the target substrates around  $\text{TiO}_2$  particles, many attempts have been performed to modify the surface or bulk properties, including the use of inert supports such as microporous zeolites (ZSM-5 [25,28], mordenite [27], zeolites A [25], X and Y [30], etc.), activated carbon [27], alumina [25], silica [25,27], mesoporous silica MCM-41 [30] and SBA-15 [31], etc.;  $\text{Al}_2\text{O}_3$ - [17],  $\text{SiO}_x$ - [32],  $\text{MgO}_x$ -modified [33] surface  $\text{TiO}_2$ ;  $\text{TiO}_2$ - $\text{SiO}_2$  and  $\text{TiO}_2$ - $\text{Al}_2\text{O}_3$  composites [14,26]; etc. Therefore, most of the photocatalytic activities were enhanced. In addition, it has found that the highest rate was observed at the supports of moderate adsorbability [27]. Even so, some shortcomings are still not overcome, such as (1) the surfaces of the supports were partially covered by  $\text{TiO}_2$  particles, causing the decrease of the initial surface areas; (2) The distributive non-uniformity of  $\text{TiO}_2$  particles on the supports; (3) many pores of supports were blocked by  $\text{TiO}_2$  particles, lowering surface area, and then both the adsorptive and photocatalytic efficiencies; etc.

It is well documented that the photocatalytic efficiency of  $\text{TiO}_2$  is greatly influenced by its phase, structure, crystallinity, particle size, surface area, porosity and surface hydroxyl groups [23,30,34], etc. Anatase nanocrystals exhibit the highest activity among three crystalline phases [15,23,34]. The higher the crystallinity, the higher the photocatalytic activity is [12,23]. Increasing the surface area is the most obvious means of improving the efficiency [23,30]. Recently, the successful preparation of mesoporous  $\text{TiO}_2$  can provide not only high surface area, but also large pores allowing a smooth diffusion of reactive molecules [23,29]. Unfortunately, it is still difficult to synthesize mesoporous  $\text{TiO}_2$  with high crystallization and large surface area [12,15].

In this paper, ordered 2-D hexagonal mesoporous  $\text{TiO}_2$ - $\text{SiO}_2$  nanocomposites with uniform and large pore channels ( $>4.0$  nm), and high surface areas ( $>70$   $\text{m}^2$   $\text{g}^{-1}$ ) have been synthesized by organic-solvent evaporation induced co-assembly method, using triblock copolymer as a template under an acidic condition [35]. Importantly, the mesopore frameworks consist of anatase  $\text{TiO}_2$  nanocrystals and amorphous  $\text{SiO}_2$  nanomatrixes, which link mutually and coexist to form unique nanocomposite, possessing coupled performances of “adsorption–photocatalysis oxidation” and providing unprecedented spaces for “the synchronous role”. Moreover, the high accessible surface areas can provide more adsorptive and photocatalytically active sites; and the large mesopore channels allow the reactive molecules to easily diffuse before and after the reactions. Our strategy realizes the synchronous role of coupled adsorption and photocatalytic oxidation by adjusting Ti/Si ratios, the number of surface hydroxyl groups, the

size and crystallinity of the anatase nanocrystallites. The cationic rhodamine-B (RhB) dye is used as the target pollutant in aqueous media. Our results demonstrate that the synchronous role generates excellent photocatalytic activity.

## 2. Experimental and characterization

### 2.1. Initial materials

Titanium isopropoxide [ $\text{Ti}(\text{OCH}(\text{CH}_3)_2)_4$ , TIPO] and tetraethyl orthosilicate [ $\text{Si}(\text{OC}_2\text{H}_5)_4$ , TEOS] were purchased from Fluka. Triblock poly(ethylene oxide)-b-poly(propylene oxide)-b-poly(ethylene oxide) copolymer, Pluronic P123 [ $M_w = 5800$ ,  $\text{HO}(\text{CH}_2\text{CH}_2\text{O})_{20}(\text{CH}_2\text{CH}_2\text{CH}_2\text{O})_{70}(\text{CH}_2\text{CH}_2\text{O})_{20}\text{H}$ ,  $\text{EO}_{20}\text{PO}_{70}\text{EO}_{20}$ , abbreviated as P123] was received from Aldrich. Ethanol, concentrated HCl (36.5 wt.%) were purchased from Shanghai Chemical Corp. Commercial P25 photocatalyst (A nanocrystalline  $\text{TiO}_2$  consisting of ca. 80% anatase and 20% rutile; average nanocrystal size:  $\sim 30$  nm; surface area:  $\sim 50$   $\text{m}^2$   $\text{g}^{-1}$ ) was kindly supplied by Degussa Corp. Rhodamine-B (RhB,  $\text{C}_{28}\text{H}_{31}\text{ClN}_2\text{O}_3$ ) was bought from Sigma-Aldrich. All the chemicals were used as received without further purification.

### 2.2. Preparation of mesoporous $\text{TiO}_2$ - $\text{SiO}_2$ composites

The ordered 2-D hexagonal mesoporous  $\text{TiO}_2$ - $\text{SiO}_2$  composites were synthesized according to our previous procedures [35]. The syntheses were carried out *via* a modified solvent EISA method under the presence of concentrated HCl and ethanol, by using TIPO and TEOS as the precursors and P123 as a structure-directing agent. For a typical synthesis, 1.0 g of P123 was dissolved in 30 g of ethanol, then 1.8 g of concentrated HCl was slowly added with vigorous stirring. After heated in a sealed bottle at  $40^\circ\text{C}$  for 3 h, 2.34 g of TIPO and 0.434 g of TEOS were added with vigorous stirring for 5 h at  $40^\circ\text{C}$ . The sols were transferred into Petri dishes, and evaporated at  $35^\circ\text{C}$  in air with the relative humidity of 50–60% for about 4 days, the resulting transparent membranes were dried at  $80^\circ\text{C}$  for 6 days. The samples were calcined at  $400^\circ\text{C}$  for 6 h in air to remove organic templates, subsequently, crystallized at  $650$ – $940^\circ\text{C}$  for 2–4 h in air with a heating rate of  $1^\circ\text{C}/\text{min}$ . The final products ( $80\text{TiO}_2$ - $20\text{SiO}_2$ ) with Ti/Si ratio of 4 were obtained. For comparison, ordered 2-D hexagonal mesoporous pure  $\text{TiO}_2$  and  $\text{SiO}_2$  were prepared using a similar procedure (see Supplementary Materials).

### 2.3. High-resolution transmission electron microscopy (HRTEM)

HRTEM images were obtained on a JEM-2011 transmission electron microscope (JEOL Company) combined with energy dispersive X-ray spectroscopy (EDX) operating at 200 kV. For HRTEM measurements, the samples were prepared by sonication in ethanol and suspended on holey carbon grids.

### 2.4. Fourier-transform infrared (FT-IR)

The investigations of surface hydroxyl groups and acidic properties of the samples were performed on a Nicolet Fourier-transform infrared (FT-IR) NEXUS 470 spectrometer using a quartz IR cell equipped with  $\text{CaF}_2$  windows. The finely ground samples (6.4–22.5 mg) were pressed into uniform self-supporting wafers and then placed into the holder. The samples were degassed at  $300^\circ\text{C}$  under a vacuum ( $<1 \times 10^{-3}$  Torr) for 4 h to remove water and other impurities, and then cooled down to room temperature (ca.  $20^\circ\text{C}$ ). Before adsorbing pyridine, the spectra were recorded to evaluate the number of surface hydroxyl groups. The samples were then exposed to a saturated vapor of pyridine at room temperature ( $20^\circ\text{C}$ ) for 20 min, thereafter, degassed at 150, 250 and  $300^\circ\text{C}$  under the vacuum for 30 min.

### 2.5. Ultraviolet–visible diffuse reflectance spectra (UV–vis DRS)

UV–vis DRS were obtained with a JASCO V-550 UV–vis spectrophotometer equipped with integrating sphere attachment using BaSO<sub>4</sub> as a reference.

### 2.6. Adsorption and photocatalytic oxidation

The performances of adsorption and photocatalytic oxidation were evaluated using aqueous solution of RhB ( $1 \times 10^{-5}$  M) in a quartz vessel at room temperature. 50 mL of RhB aqueous solution and 50.0 mg of the finely ground mesoporous TiO<sub>2</sub>–SiO<sub>2</sub> composite powders were placed in a quartz vessel, which formed a suspension under stirring. For comparison, all the experiments were carried out under the identical conditions. The suspensions were stirred first in dark for a certain time to evaluate the adsorption performance. After establishing adsorption–desorption equilibrium, UV light irradiation was turned on. The photocatalytic reactions were carried out under UV light irradiation from a 25 W low-pressure mercury lamp ( $\lambda = 254$  nm). The radiant flux was measured with a photometer (International Light Model IL1400A). About 1.0 mL of suspensions were taken at given time intervals and centrifuged at 15,000 rpm for 10 min. The concentration of RhB was analyzed using a Thermo-Spectronic UV 500 UV–vis spectrometer, and the variations of the absorption at 554 nm were recorded. For comparison, the performances of mesoporous TiO<sub>2</sub> crystallized at 800 °C for 2 h (TiO<sub>2</sub>-800), commercial P25, and mesoporous SiO<sub>2</sub> calcined at 800 °C for 2 h were also measured. Under the conditions of measurement, the concentration change of RhB follows Lambert–Beer's law. It should be mentioned that the mesoporous samples used herein were ground far finer than that used in our previous paper [35]. Thus, the performances were closer to their facts.

### 2.7. Chemical oxygen demand (COD<sub>Cr</sub>)

CODs of five different suspensions containing the representative 80TiO<sub>2</sub>–20SiO<sub>2</sub>-900 composites and their corresponding initial aqueous solutions of RhB ( $1.8 \times 10^{-5}$ ,  $2 \times 10^{-5}$ ,  $3 \times 10^{-5}$ ,  $5 \times 10^{-5}$  and  $1 \times 10^{-4}$  M) were directly analyzed using the standard potassium dichromate titration method [36], respectively. For comparison, the suspensions tested for COD were prepared under the identical conditions as that of the above adsorption and photocatalytic oxidation, and as each other except for RhB concentration. Here, it should be indicated that we selected  $1 \times 10^{-5}$  M RhB solution to highlight our proposed “synchronous role” in this paper, mainly because that both the processes of adsorption and photocatalytic oxidation can be more clearly distinguished for all the samples investigated.

## 3. Results

### 3.1. HRTEM images

HRTEM images reveal that the frameworks of mesoporous TiO<sub>2</sub>–SiO<sub>2</sub> composites consist of anatase nanocrystals and amorphous SiO<sub>2</sub> nanoparticles (Fig. 1), which link mutually and coexist to form unique nanocomposites. The lattice fringes of nanocrystals can be clearly observed, which are randomly oriented and overlapped each other. The average size of nanocrystals evaluated is in the range of 7–16.5 nm (Table 1), which decreases with the decrease of Ti/Si ratio (Fig. 1a–d). Both the size and crystallinity of nanocrystals increase with the rise of crystallizing temperature (Fig. 1e, b, f, and g). With the coarsening of nanocrystals, more and more nanocrystals pierce into the channels, however, they are still connected with SiO<sub>2</sub> nanoparticles. Both the number and size of SiO<sub>2</sub> nanoparticles increase with the decrease of Ti/Si ratio. The size enlarges as the

crystallizing temperature rise, implying the adsorption centers increase. The mesopore channels are large, ordered and uniform. The mean pore size evaluated is in the range of 4.3–7.4 nm (Table 1), which overall decreases with the rises of Ti/Si ratio and temperature. The biggest pore size with thick pore wall is about 12.6 nm (Fig. 1e), which is the critical size of nanocrystals in our samples, otherwise the mesostructures would fully collapse. The mesostructure of 80TiO<sub>2</sub>–20SiO<sub>2</sub> composite crystallized at 940 °C has already completely collapsed (Fig. 1g), resulted in by the larger nanocrystals (ca. 16.5 nm) than the critical size. In addition, the specific surface areas of the composites before the complete collapse of mesostructures are high ( $>70$  m<sup>2</sup> g<sup>−1</sup>) (Tables 1 and 2; Fig. S1).

### 3.2. FT-IR spectra

FT-IR spectrum of TiO<sub>2</sub>-800 sample (Fig. 2Aa, Fig. S2) shows no obvious absorbance band, clearly suggesting there are few hydroxyls on surface, because the Ti–OH groups are unstable and dehydroxylated at 180 °C [37–38]. For the mesoporous 90TiO<sub>2</sub>–10SiO<sub>2</sub> composite crystallized at 800 °C (90TiO<sub>2</sub>–10SiO<sub>2</sub>-800), an band of Si–OH stretching vibration appears in the range of 3800–3600 cm<sup>−1</sup> (centered at  $\sim 3740$  cm<sup>−1</sup>) (Fig. 2Ab) [39–40], indicating that some silicon atoms are located on the surface. The area of hydroxyl band increases with the decrease of Ti/Si ratio (Fig. 2Ab–e; Table 1), suggesting an increase of adsorption centers. Very interestingly, when Ti/Si ratio is fixed, such as 80/20, the number of silanol groups first increases significantly with the temperature rise, then dramatically declines at 940 °C (Fig. 2B, Table 1) due to the complete collapse of mesostructure (Fig. 1g, Figs. S3 and S4). As the temperature elevates, the small TiO<sub>2</sub> nanocrystals in the frameworks grow up large ones; meanwhile, some of the small TiO<sub>2</sub> nanocrystals are consumed as the building blocks of large ones. During this process, more nanosized SiO<sub>2</sub> particles among the small TiO<sub>2</sub> nanocrystals are progressively exposed and simultaneously aggregate into larger ones, which result in the increase of surface Si–OH groups before the full mesostructural collapse. In addition, a surface rich in Si is energetically more favorable than rich in Ti [38].

FT-IR spectra of pyridine adsorption show no adsorption peak for the TiO<sub>2</sub>-800 sample (Fig. 3A), suggesting a very low acidity [41]. Differently, the 90TiO<sub>2</sub>–10SiO<sub>2</sub>-800 shows several characteristic bands (Fig. 3Ba), which are assigned to the pyridine adsorbed on Lewis acid sites (exposed Ti<sup>4+</sup> cations, 1444 and 1605 cm<sup>−1</sup>), Brönsted acid sites (associated with Ti–O–Si bridges, 1541 and 1637 cm<sup>−1</sup>) [41–42]. With desorption temperature rise, the intensity of peaks decreases (Fig. 3Bb and Bc; Table 1), however, they are still observed at 300 °C, indicating a strong surface acidity [41–42]. The similar observation is obtained for other mesoporous TiO<sub>2</sub>–SiO<sub>2</sub> composites (Fig. 3C–F, Table 1). The numbers of Lewis and total acid sites (TAS, both the Lewis and Brönsted acid sites) decrease with the decrease of Ti/Si ratio, perhaps resulted from the decrease of the exposed Ti atoms on the surface [38]. Whereas the number of Brönsted acid sites increases, caused by the increased Ti–O–Si chemical bonds on the surface [38]. Both L and B, and TAS decrease with the temperature elevation, which are perhaps caused by both the decreases of the exposed Ti atoms and Ti–O–Si linkages on the surface due to the enlargements of both anatase nanocrystals and SiO<sub>2</sub> nanoparticles, and the decline of specific surface area (Fig. S1). All the above results imply that the adsorption centers from acidities decrease [41].

### 3.3. UV–vis DRS

All the mesoporous TiO<sub>2</sub>–SiO<sub>2</sub> composites with different Ti/Si ratios display similar UV–vis DRS spectra (Fig. 4), which is different with the TiO<sub>2</sub>-800 sample (Fig. 4Aa). The slight blue-shift is observed with the decrease of Ti/Si ratio (Fig. 4A); while a slight



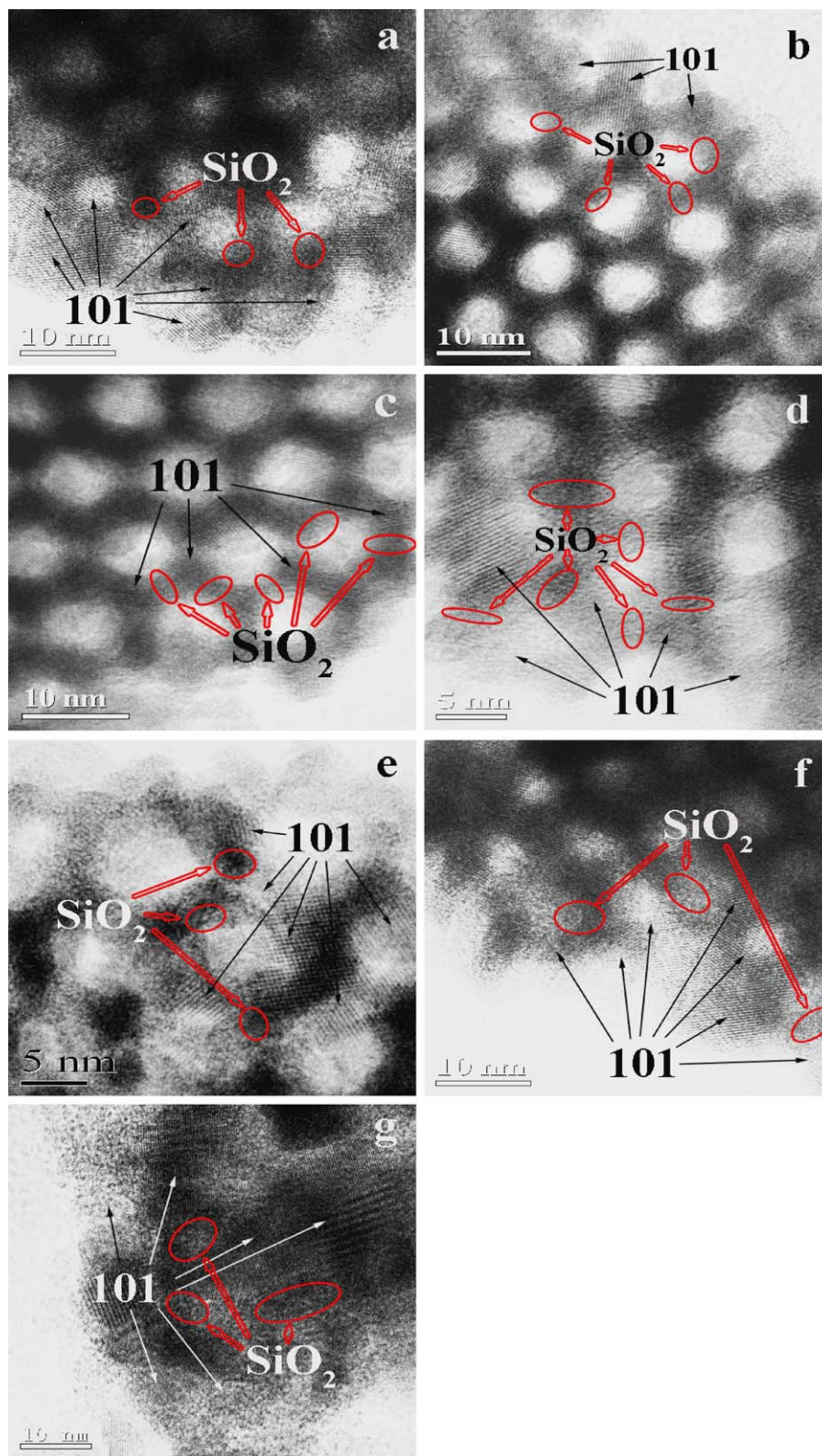


**Fig. 1.** Representative HRTEM images of 2-D hexagonal mesoporous composites of 90TiO<sub>2</sub>-10SiO<sub>2</sub> (a), 80TiO<sub>2</sub>-20SiO<sub>2</sub> (b), 70TiO<sub>2</sub>-30SiO<sub>2</sub> (c) and 60TiO<sub>2</sub>-40SiO<sub>2</sub> (d) crystallized at 800 °C for 2 h, respectively; and 2-D hexagonal mesoporous 80TiO<sub>2</sub>-20SiO<sub>2</sub> composites crystallized at 650 °C for 4 h (e), 900 °C (f) and 940 °C (g) for 2 h, respectively; viewed along [0 0 1] direction.

red-shift with the crystallizing temperature rise (Fig. 4B). It is well known that the absorption near the band edge follows the equation  $\alpha h\nu = A(h\nu - E_g)^{n/2}$ , where  $\alpha$ ,  $\nu$ ,  $A$ ,  $E_g$  and  $n$  are the absorption coefficient, the light frequency, a constant, band gap and an integer, respectively [20,43]. Here,  $n$  depends on whether the

transition is direct ( $n = 1$ ) or indirect ( $n = 4$ ) [43]. The band gaps are direct for our anatase TiO<sub>2</sub>-SiO<sub>2</sub> composites [44], since SiO<sub>2</sub> is inactive for UV-vis light [2,45] and does not change the transition of TiO<sub>2</sub>. Thus, the band gaps ( $E_g$ ) can be estimated by extrapolating to zero a linear fit to the plots of the square root of Kubelka-Munk

**Table 1**

Physicochemical properties, peak areas of surface hydroxyls and pyridine adsorbed at different desorption temperatures for the representative 2-D hexagonal mesoporous TiO<sub>2</sub>-SiO<sub>2</sub> composites prepared with different Ti/Si ratios and crystallizing temperatures.

Sample name	Temperature and time of cryst <sup>a</sup> /°C (h)	$S_{\text{BET}}^b/\text{m}^2\text{g}^{-1}$	Average pore size <sup>c</sup> /nm	Average nanocrystal size <sup>d</sup> /nm	Sample weight/mg	$S_{\text{OH}}/\text{g}^e$	Desorption temperature of pyrid <sup>f</sup> /°C	Peak areas of pyridine adsorbed		
								$S_{\text{LA}}/\text{g}^g$ 1444 cm <sup>-1</sup>	$S_{\text{BA}}/\text{g}^h$ 1541 cm <sup>-1</sup>	$S_{\text{TA}}/\text{g}^i$
TiO <sub>2</sub> -800	800 (2)	13			12.3	0	150	0	0	0
							250	0	0	0
							300	0	0	0
90TiO <sub>2</sub> -10SiO <sub>2</sub> -800	800 (2)	115	5.2	11.6	6.6	282	150	111	4	115
							250	55	2	57
							300	26	1	27
80TiO <sub>2</sub> -20SiO <sub>2</sub> -800	800 (2)	190 <sup>*</sup>	6.5	10.8	9.7	548	150	95	9	104
							250	38	3	41
							300	17	2	19
70TiO <sub>2</sub> -30SiO <sub>2</sub> -800	800 (2)	217 <sup>*</sup>	7.0	9.2	7.2	784				
60TiO <sub>2</sub> -40SiO <sub>2</sub> -800	800 (2)	231 <sup>*</sup>	6.7	7.1	7.0	878	150	67	14	81
							250	23	9	32
							300	8	7	15
80TiO <sub>2</sub> -20SiO <sub>2</sub> -650	650 (4)	236 <sup>*</sup>	7.4	8.0	11.2	126	150	124	16	140
							250	65	10	75
							300	35	7	42
80TiO <sub>2</sub> -20SiO <sub>2</sub> -750	750 (2)	204 <sup>*</sup>			6.4	375				
80TiO <sub>2</sub> -20SiO <sub>2</sub> -800	800 (2)	190 <sup>*</sup>	6.5	10.8	9.7	548	150	95	9	104
							250	38	3	41
							300	17	2	19
80TiO <sub>2</sub> -20SiO <sub>2</sub> -900	900 (2)	73 <sup>*</sup>	4.3	12.9	13.7	801	150	27	3	30
							250	14	2	16
							300	8	1	9
80TiO <sub>2</sub> -20SiO <sub>2</sub> -940	940 (2)	20		16.5	22.5	518				

<sup>a</sup> Temperature and time of crystallizing.

<sup>b</sup> BET specific surface area, the data with asterisks were taken from Reference [35].

<sup>c</sup> The average pore sizes were obtained by measuring the size of the pores from the HRTEM images.

<sup>d</sup> The data were obtained by measuring the size of nanocrystals from the HRTEM images.

<sup>e</sup> Peak area of surface hydroxyl groups per gram of sample calculated from the integrated areas of FT-IR spectra and sample weight.

<sup>f</sup> Desorption temperatures of pyridine.

<sup>g</sup> Peak area of pyridine adsorbed on Lewis acid sites per gram of sample.

<sup>h</sup> Peak area of pyridine adsorbed on Brönsted acid sites per gram of sample.

<sup>i</sup> Peak area of pyridine adsorbed on total acid sites per gram of sample (Lewis and Brönsted acids,  $S_{\text{LA}} + S_{\text{BA}}$ ).

<sup>\*</sup> Data taken from Ref. [35].

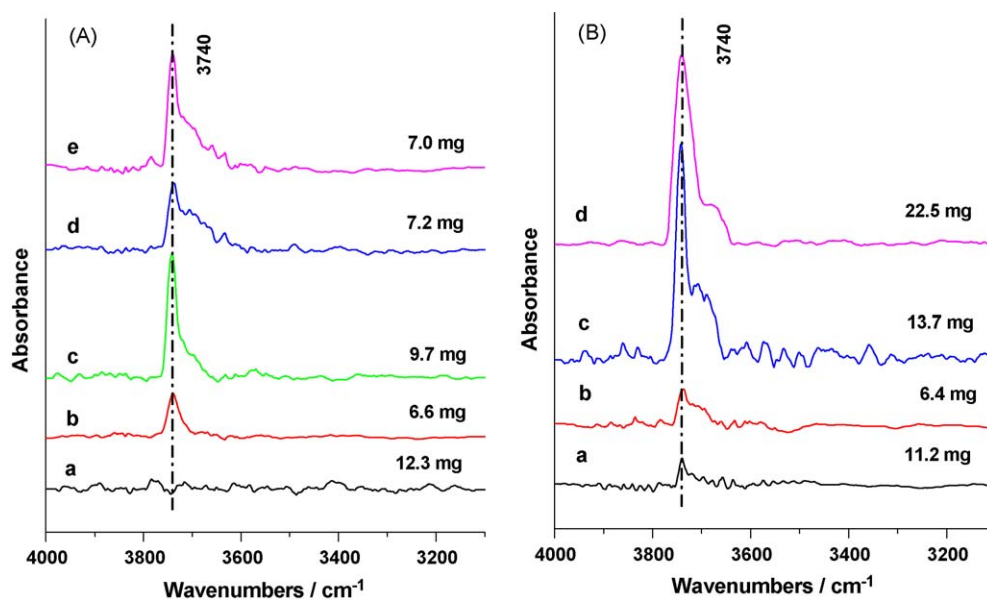


**Fig. 2.** Transmission *in situ* FT-IR spectra in the OH stretching region for representative 2-D hexagonal mesoporous TiO<sub>2</sub>-SiO<sub>2</sub> composites with different Ti/Si ratios crystallized at 800 °C for 2 h (A), respectively: (a) TiO<sub>2</sub>, (b) 90TiO<sub>2</sub>-10SiO<sub>2</sub>, (c) 80TiO<sub>2</sub>-20SiO<sub>2</sub>, (d) 70TiO<sub>2</sub>-30SiO<sub>2</sub> and (e) 60TiO<sub>2</sub>-40SiO<sub>2</sub>; and 2-D hexagonal mesoporous 80TiO<sub>2</sub>-20SiO<sub>2</sub> composites (B) crystallized at 650 °C for 4 h (a), 750 °C (b), 900 °C (c) and 940 °C (d) for 2 h, respectively.

functions against  $h\nu$  of the light [20,46–47], as presented in Fig. 4C and D. The gaps of mesoporous  $\text{TiO}_2\text{-SiO}_2$  composites are larger than that of  $\text{TiO}_2\text{-800}$  and P25, which slightly increases with the decrease of Ti/Si ratio and decreases with the temperature rise.

### 3.4. Adsorption performance

The adsorptive and photocatalytic performances of mesoporous  $\text{TiO}_2\text{-SiO}_2$  composites with various Ti/Si ratios ( $\infty$ , 90/10, 80/20, 70/

30, 60/40 and 0) were evaluated in RhB aqueous solution ( $1 \times 10^{-5}$  M) at room temperature. Before UV irradiation, an adsorption process of RhB on the samples occurs. The process proceeds very fast, it takes about 5 min close to saturation and  $\sim 15$  min to reach adsorption–desorption equilibration for most of the samples (Fig. 5A and B, Fig. S5A–C). The saturated adsorption amounts (SAA) on both commercial P25 and  $\text{TiO}_2\text{-800}$  samples (Fig. 5Aa–b) are very low, clearly suggesting a weak interaction of  $\text{TiO}_2$  with RhB. Interestingly, mesoporous  $\text{TiO}_2\text{-SiO}_2$  composites

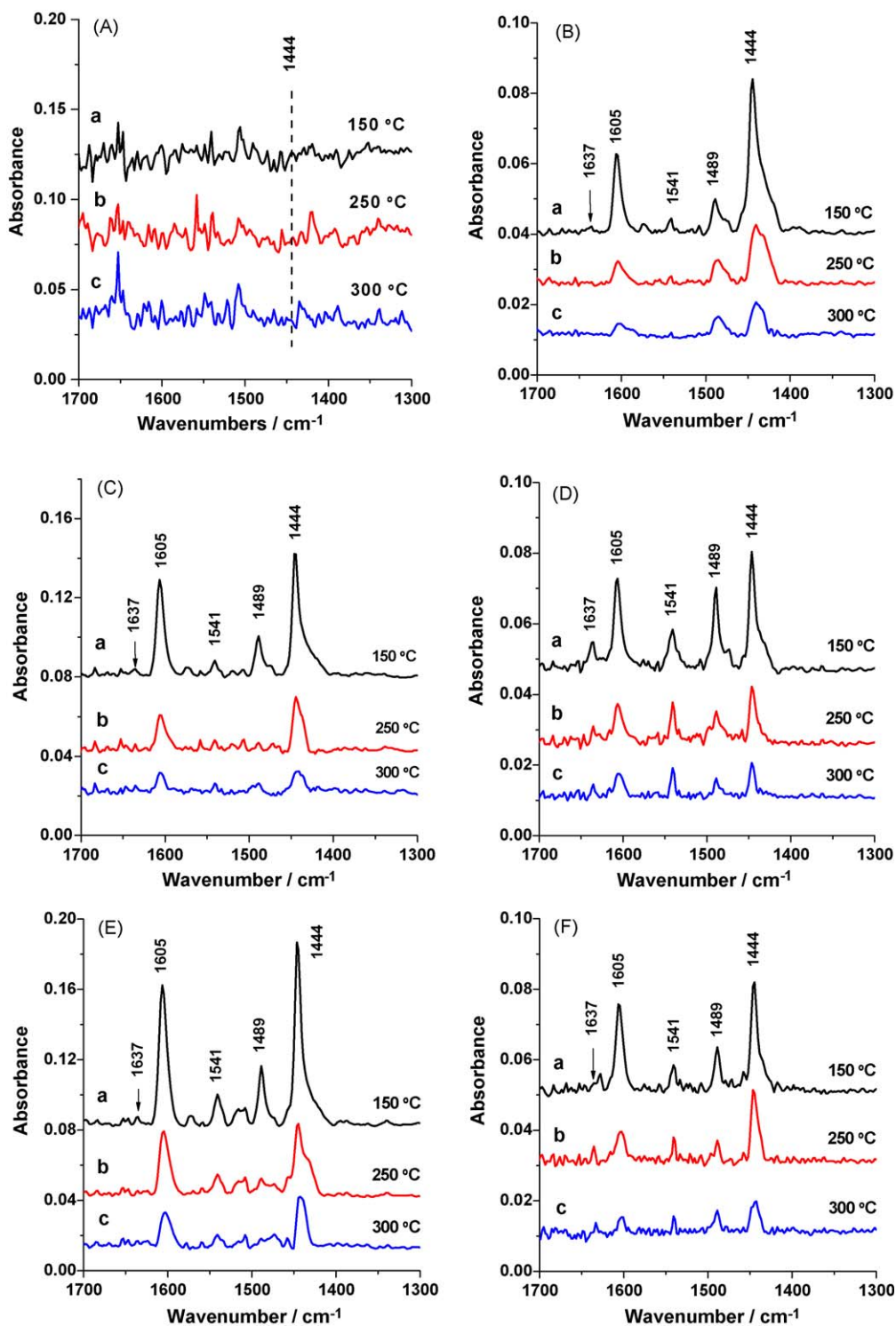


**Fig. 3.** *In situ* FT-IR spectra of pyridine adsorbed on the representative samples after evacuation at 150, 250, and 300 °C: (A) mesoporous pure  $\text{TiO}_2$  crystallized at 800 °C for 2 h; (B–D) mesoporous 90 $\text{TiO}_2$ –10 $\text{SiO}_2$ , 80 $\text{TiO}_2$ –20 $\text{SiO}_2$  and 60 $\text{TiO}_2$ –40 $\text{SiO}_2$  composites crystallized at 800 °C for 2 h, respectively; (E and F) mesoporous 80 $\text{TiO}_2$ –20 $\text{SiO}_2$  composites crystallized at 650 °C for 4 h and 900 °C for 2 h, respectively.



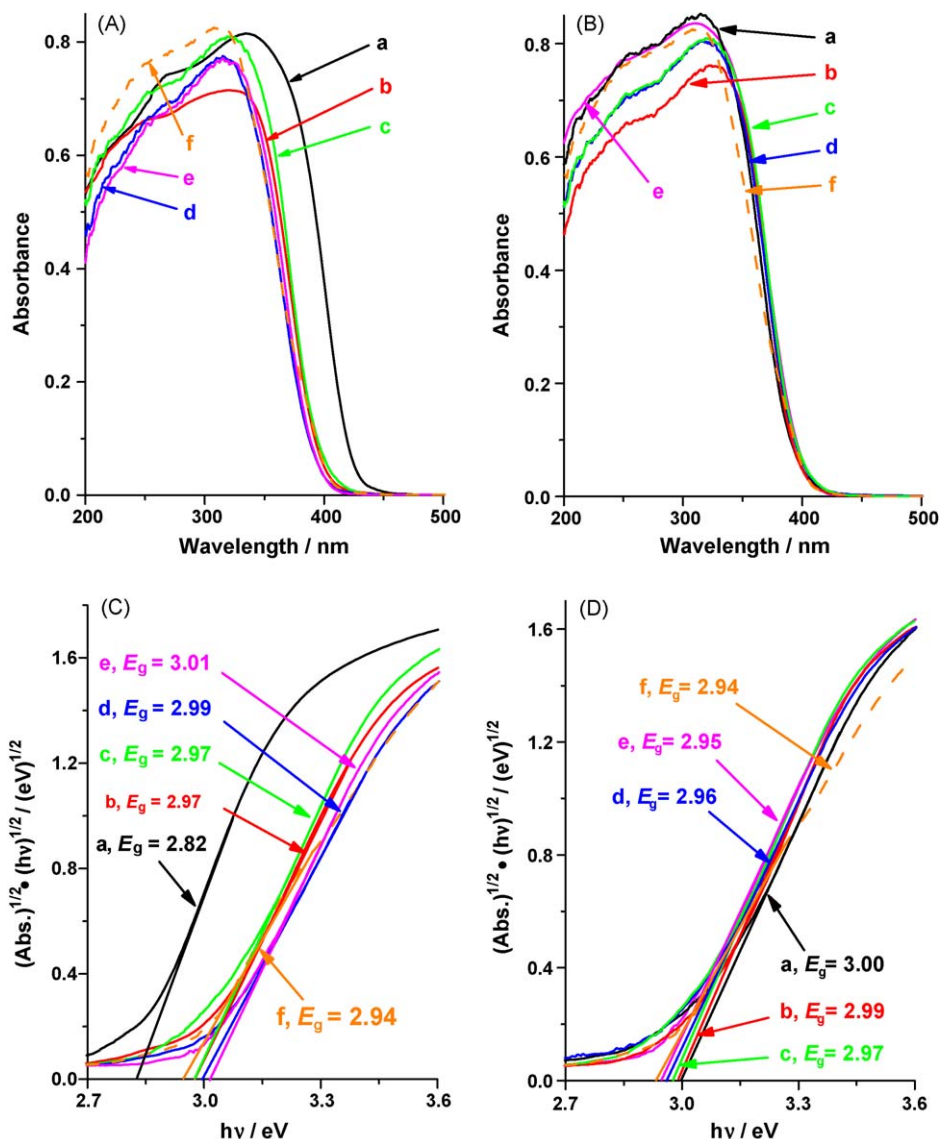


**Fig. 4.** UV-vis DRS of the representative 2-D hexagonal mesoporous  $\text{TiO}_2$ - $\text{SiO}_2$  composites with different Ti/Si ratios crystallized at 800 °C for 2 h (A and C), respectively, (a) pure  $\text{TiO}_2$ , (b) 90 $\text{TiO}_2$ -10 $\text{SiO}_2$ , (c) 80 $\text{TiO}_2$ -20 $\text{SiO}_2$ , (d) 70 $\text{TiO}_2$ -30 $\text{SiO}_2$ , (e) 60 $\text{TiO}_2$ -40 $\text{SiO}_2$ ; and mesoporous 80 $\text{TiO}_2$ -20 $\text{SiO}_2$  composites (B, D) crystallized at 650 °C for 4 h (a), 750 °C (b), 800 °C (c), 900 °C (d), 940 °C (e) for 2 h, respectively; (f) P25 photocatalyst. (A and B) Absorbance versus light wavelength; (C and D) the square root of Kubelka-Munk functions against  $h\nu$  of the light.

exhibit excellent adsorbability for RhB, which are much higher than that of P25 and  $\text{TiO}_2$ -800. The adsorption performances significantly enhance with the decrease of Ti/Si ratio (Fig. 5A). This trend is similar to that of the samples crystallized at other temperatures (Fig. S5D). More interestingly, the adsorption performances greatly increase first with crystallizing temperature rise, then dramatically decline at 940 °C (Fig. 5B), due to the full collapse of mesostructure (Fig. 1g, Fig. S3). The samples with different Ti/Si ratios exhibit the similar trend (Fig. S5), but the threshold increases with the decline of Ti/Si ratio. The largest adsorption amount (100%) occurs on the mesoporous  $\text{SiO}_2$  (Fig. 5Ag,  $S_{\text{BET}} = 269 \text{ m}^2 \text{ g}^{-1}$ , Fig. S6).

### 3.5. Photocatalytic oxidation performance

On irradiation of UV light, the concentration of RhB decreases exponentially with the time for the samples except for the  $\text{TiO}_2$ -800 (Fig. 5A and B, Fig. S5A–C). The pseudo-first-order reactions are observed (Fig. 5C and D, Fig. S7A–C). The activities decline with the decrease of Ti/Si ratio when the composite samples crystallized at

800 °C (Fig. 5C). This trend is also observed on the samples crystallized at other temperatures (Fig. S7D) except for the 90 $\text{TiO}_2$ -10 $\text{SiO}_2$  composite crystallized at 900 °C, due to the collapse of mesostructure (Figs. S8 and S9). Noteworthy, the activities of all the composites investigated are far higher than that of  $\text{TiO}_2$ -800 ( $0.00587 \text{ min}^{-1}$ , Fig. 5Cb). In addition, most of the activities are distinctly higher than that of commercial P25 photocatalyst ( $0.0671 \text{ min}^{-1}$ , Fig. 5Ca). Very significantly, when Ti/Si ratio is fixed, such as 80/20, the activities increase remarkably first with the temperature elevation, and reach the highest value ( $0.231 \text{ min}^{-1}$ ) at 900 °C, which is much higher than that for P25, then decrease sharply at 940 °C (Fig. 5B and D). The samples with different Ti/Si ratios present the similar trend (Fig. S7D), but the threshold increases with the decrease of Ti/Si ratio.

### 3.6. COD

The percentage of COD removal increases with the decrease of initial concentration of RhB (Fig. 6). When the initial concentration

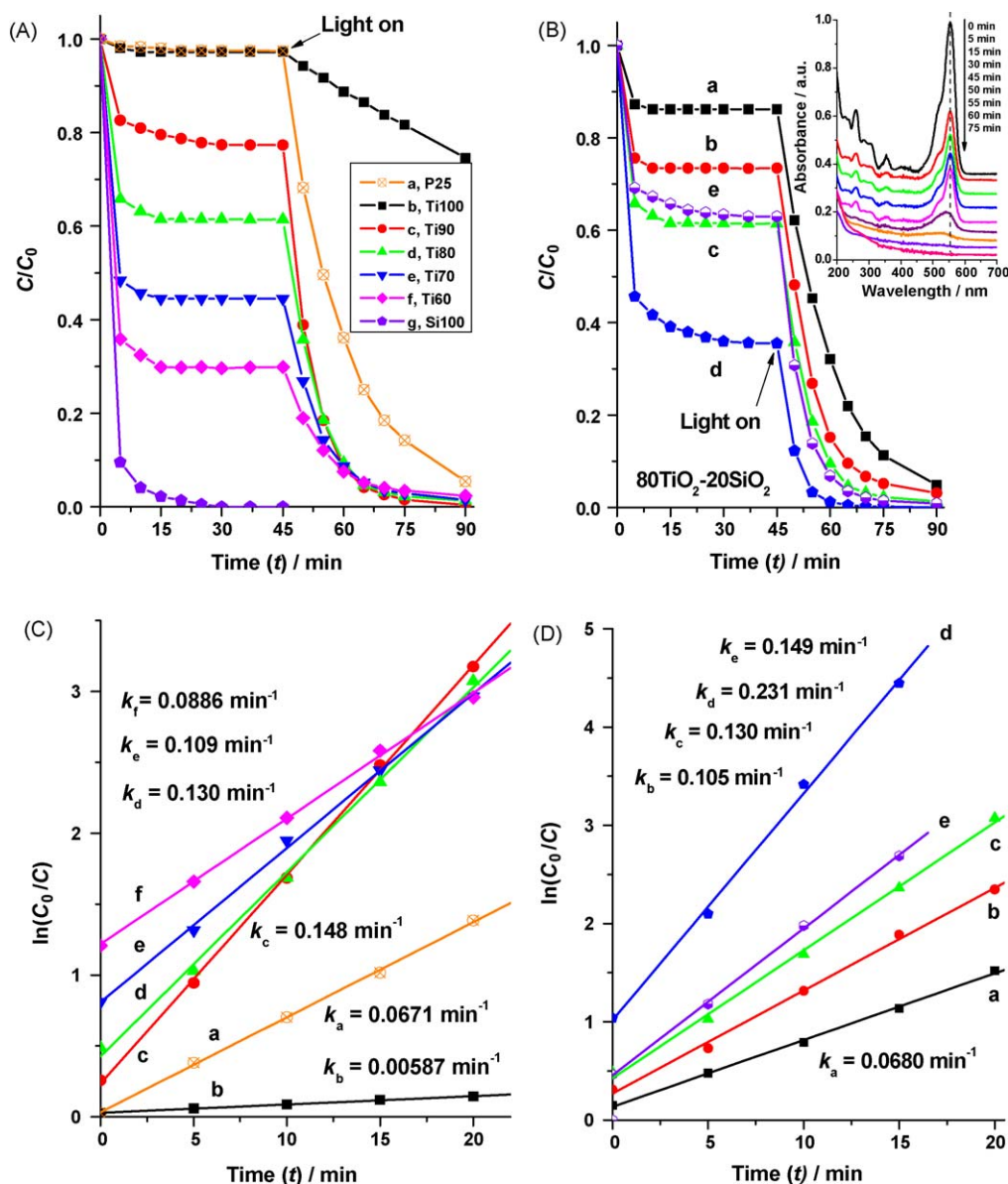


**Fig. 5.** (A and B) Performances of adsorption and photocatalytic oxidation of RhB monitored as the normalized concentration change versus time of adsorption before UV irradiation and photocatalytic reaction under UV irradiation in the presence of samples; here,  $C$  is the concentration of RhB at the time  $t$  and  $C_0$  is the initial concentration. (C and D) Photocatalytic oxidation of RhB monitored as the  $\ln(C_0/C)$  versus UV irradiation time in the presence of samples. (A and C) (a) P25 photocatalyst, (b–g) 2-D hexagonal mesoporous TiO<sub>2</sub>-SiO<sub>2</sub> composites with different Ti/Si ratios crystallized at 800 °C for 2 h, respectively, (b) pure TiO<sub>2</sub>, (c) 90TiO<sub>2</sub>-10SiO<sub>2</sub>, (d) 80TiO<sub>2</sub>-20SiO<sub>2</sub>, (e) 70TiO<sub>2</sub>-30SiO<sub>2</sub>, (f) 60TiO<sub>2</sub>-40SiO<sub>2</sub> and (g) pure SiO<sub>2</sub>. (B and D) 2-D hexagonal mesoporous 80TiO<sub>2</sub>-20SiO<sub>2</sub> composites crystallized at 650 °C for 4 h (a), 750 °C (b), 800 °C (c), 900 °C (d) and 940 °C (e) for 2 h, respectively. (B, inset) Representative UV-vis spectral changes of RhB aqueous solution in the presence of 80TiO<sub>2</sub>-20SiO<sub>2</sub>-900 composite, corresponding to the data in (B).

of RhB is lower than  $3 \times 10^{-5} \text{ M}$ , the percentage of COD removal rises rapidly. These results clearly indicate that the RhB dye was not only decolorized but also degraded by our mesoporous TiO<sub>2</sub>-SiO<sub>2</sub> composites.

## 4. Discussion

### 4.1. Adsorption performance

Although the change of adsorption performance with the declining of Ti/Si ratio is consistent with that of their surface areas (Fig. S1), they are right opposite with the temperature rise before the collapse of mesostructures, evidently suggesting non-relativity between them. Interestingly, the trend of adsorption performance greatly agrees with that of Si-OH groups, clearly indicating a relationship between them. To further confirm it, the adsorbability

of mesoporous SiO<sub>2</sub> prepared by the similar procedure was also evaluated. As expected, the mesoporous SiO<sub>2</sub> exhibits large adsorption capability, mainly due to the numerous surface silanol groups [39–40]. Noticeably, the enhancement of adsorption performance disagrees with the decrease of TAS, illustrating no correlation between them. The results clearly demonstrate that the adsorption of RhB on our samples is overwhelmingly driven by the Si-OH groups. In addition, the mesostructural integrity is also very important.

### 4.2. Photocatalytic degradation activities

The activities enhance with the increase of the size and crystallinity of anatase nanocrystals, and the decrease of band gaps under maintaining the mesostructural integrity. However, the change of activities is fully opposite to that of their surface areas,



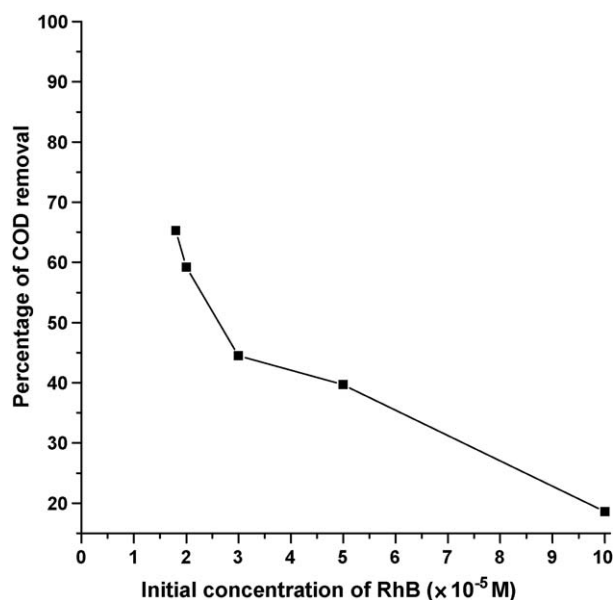


**Fig. 6.** Relationship of percentage of COD removal with the initial concentration of RhB aqueous solution. The representative mesoporous  $80\text{TiO}_2\text{-}20\text{SiO}_2\text{-}900$  composite was used as the photocatalyst.

showing a non-correlativity between them. It is noteworthy that although the trend of activity with the decrease of Ti/Si ratio is coincident with that of TAS, they are just contrary with the temperature rise, clearly suggesting there is no correlation between them in our samples.

#### 4.3. Synchronous role

The perfect combinations of anatase nanocrystals and  $\text{SiO}_2$  nanoparticles on our unique mesoporous frameworks provide unprecedented spaces for “the synchronous role of coupled adsorption and photocatalytic oxidation”. When crystallizing temperature is fixed, under maintaining the mesostructures, the adsorption role dramatically enhances with the decrease of Ti/Si ratio, whereas the role of photocatalytic oxidation declines due to the decrease of nanocrystals resulting in the increased band gaps. Accordingly, the activities decline pronouncedly due to far from the synchronous role. Fortunately, before the mesostructural collapse, when Ti/Si ratio is fixed, both the roles obviously enhance with the crystallizing temperature elevation. Therefore, the activities remarkably enhance as a result of the synergistic role. Our strategy is to realize the synchronous role to obtain the excellent activity by adjusting Ti/Si ratios, the hydroxyl groups, the size and crystallinity of nanocrystals on the unique frameworks.

An ideal material would be one in which the nanocrystals are large enough to give bulk anatase behavior (e.g., no quantum effects that increase the band gap) [26]. Theoretically, the critical size of nanocrystals in our samples is about 12.6 nm. Fortunately, the nanocrystals sizes in the  $90\text{TiO}_2\text{-}10\text{SiO}_2\text{-}850$  and  $80\text{TiO}_2\text{-}20\text{SiO}_2\text{-}900$  are 12.7 and 12.9 nm (Tables 1 and 2), respectively, which are nearly the same as each other and as 12.6 nm. Their surface areas ( $81$  and  $73\text{ m}^2\text{ g}^{-1}$ , respectively) are also very close to each other. However, their rate constants ( $0.194$  and  $0.231\text{ min}^{-1}$ , respectively) have a big difference, which is probably caused by their different adsorption performances. The adsorption performance of the latter is much higher than that of the former, accordingly the adsorption role of the latter approached synchronicity with the oxidation role, leading to the higher activity. When the nanocrystals sizes are larger than *ca.* 12.6 nm, such as 15.1 and/or 15.4 nm (Table 2), the mesostructures have already fully collapsed. In these circumstances, the synchronicity evidently declines, causing the decrease of activities. With the lowering in the Ti/Si ratio, such as  $70\text{TiO}_2\text{-}30\text{SiO}_2\text{-}900$  composite, the adsorption role is stronger than that of  $80\text{TiO}_2\text{-}20\text{SiO}_2\text{-}900$ , but the role of photocatalytic oxidation is weaker than that of the latter caused by the decrease of nanocrystals. Thus, the activity declines owing to away from the synchronous role. As the Ti/Si ratio further decreases, such as  $60\text{TiO}_2\text{-}40\text{SiO}_2\text{-}800$  and  $60\text{TiO}_2\text{-}40\text{SiO}_2\text{-}900$  composites, although the adsorption performances enhance greatly, the activities continue to decline obviously thanks to far from the synchronous role. When the crystallization temperature is elevated to higher than  $900^\circ\text{C}$ , though both the roles co-enhance for the mesoporous  $70\text{TiO}_2\text{-}30\text{SiO}_2$  and  $60\text{TiO}_2\text{-}40\text{SiO}_2$  composites, the rate constants (no shown here) are still lower than  $0.231\text{ min}^{-1}$ . Therefore, the highest activity ( $0.231\text{ min}^{-1}$ ) on our samples is much higher than that on P25 ( $0.0671\text{ min}^{-1}$ ). Our results demonstrate that the synchronous role is key factor to the excellent activity.

#### 4.4. Process of synchronous role

Our results show that the whole conjugated chromophore structures of RhB were quite easily cleaved (Fig. 5B, inset), since the characteristic absorption band around 554 nm decreased rapidly during UV irradiation [18]. It was reported that the hydroxyls on the surface can bind the carboxylic group of RhB dominantly through a monodentate ester-like linkage [17–18]. The anatase nanocrystals were documented to be dominantly inside the mesochannels of mesoporous  $\text{TiO}_2$  due to the large inner surface, and the generation of  $\cdot\text{OH}$  should occur dominantly on the inner surface, which deactivates rapidly and converts to an inactive surface  $-\text{OH}$  group in a near-diffusion-controlled rate. Hence,  $\cdot\text{OH}$  scarcely diffuses out of the pores, because the diffusion distance inside the cylindrical mesopores is 1.3–2.4 nm [29]. This means that the photocatalytic reaction occurs dominantly inside the

**Table 2**

Physicochemical properties of some 2-D hexagonal mesoporous  $\text{TiO}_2\text{-SiO}_2$  composites prepared with different Ti/Si ratios and crystallizing temperatures.

Sample name	Temperature and time of cryst <sup>a</sup> /°C (h)	MP pore size <sup>b</sup> /nm	$S_{\text{BET}}^c/\text{m}^2\text{ g}^{-1}$	$V_T^d/\text{mL g}^{-1}$	Average nanocrystal size <sup>e</sup> /nm
$\text{TiO}_2\text{-}800$	800 (2)	33	13	0.060	60.0
$90\text{TiO}_2\text{-}10\text{SiO}_2\text{-}800$	800 (2)	4.6	115	0.14	10.8
$90\text{TiO}_2\text{-}10\text{SiO}_2\text{-}850$	850 (2)	4.8	81	0.11	12.7
$90\text{TiO}_2\text{-}10\text{SiO}_2\text{-}900$	900 (2)	5.0	36	0.050	15.4
$80\text{TiO}_2\text{-}20\text{SiO}_2\text{-}940$	940 (2)	3.5	20	0.026	15.1
$\text{SiO}_2\text{-}800$	800 (2)	3.8	269	0.27	

<sup>a</sup> Temperature and time of crystallization.

<sup>b</sup> The mean pore size was calculated using the BJH method from the adsorption data of  $\text{N}_2$  isotherms.

<sup>c</sup> BET specific surface area.

<sup>d</sup> Total pore volume.

<sup>e</sup> Calculated from the half-height width of the 101 and 110 diffraction peaks on the WAXRD patterns using Scherrer equation for anatase and rutile nanocrystals, respectively.

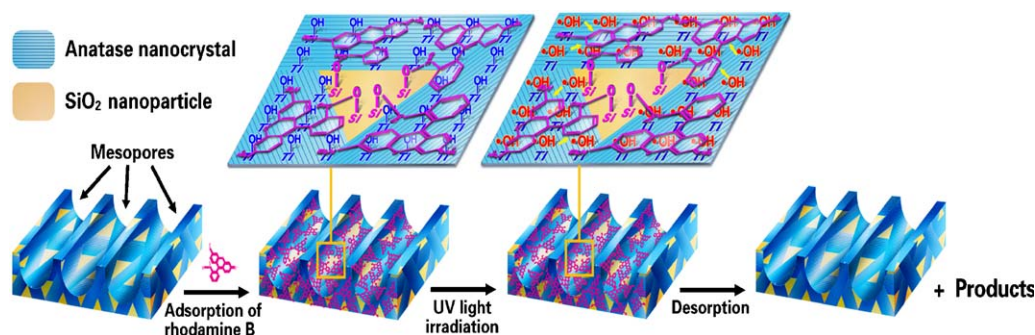


**Fig. 7.** Scheme for the synchronous role of coupled adsorption and photocatalytic oxidation of RhB dye on ordered 2-D hexagonal mesoporous anatase  $\text{TiO}_2$ - $\text{SiO}_2$  nanocomposites.

mesopores. For our mesoporous  $\text{TiO}_2$ - $\text{SiO}_2$  nanocomposites, the anatase nanocrystals and  $\text{SiO}_2$  nanoparticles similarly coexist predominantly inside the mesochannels. During the reaction,  $\text{SiO}_2$  nanoparticles adsorb RhB molecules from the aqueous solution through Si-OH groups to form monodentate ester-like linkage with the carboxylic group, the adsorbed RhB molecules then diffuse very easily into the inner surface and enrich on the  $\text{SiO}_2$  nanoparticles (Fig. 7). Meanwhile anatase nanocrystals generate  $\cdot\text{OH}$  radicals by UV irradiation, which simultaneously attack the pre-enriched RhB from many different directions. As a result, the RhB is in no time cleaved into small molecules. Subsequently, the resultants diffuse out of the pores into the solution. In this process, the  $\cdot\text{OH}$  radicals are very highly efficiently utilized because of the synchronous role of adsorption and photocatalytic oxidation, generating the excellent activity. For the heterogeneous photocatalytic reactions of other organic pollutants in water or gas phase, using UV or visible light irradiation, our work similarly has important significance.

## 5. Conclusions

The ordered 2-D hexagonal mesoporous anatase  $\text{TiO}_2$ - $\text{SiO}_2$  nanocomposites with coupled adsorption and photocatalytic oxidation have been synthesized by organic-solvent evaporation induced co-assembly approach, using TIPO and TEOS as the inorganic precursors, P123 as a template under an acidic condition. HRTEM, XRD, FT-IR, UV-vis DRS,  $\text{N}_2$  adsorption techniques have been employed to systematically investigate the structural and surface properties. The results showed that the mesopore frameworks consist of anatase  $\text{TiO}_2$  nanocrystals and amorphous  $\text{SiO}_2$  nanoparticles, which link mutually and coexist to form unique nanocomposites, possessing coupled performances of “adsorption-photocatalysis oxidation” and providing unprecedented spaces for the “synchronous role”. The number of surface Si-OH groups increases significantly with both the decrease of Ti/Si ratio and the elevation of crystallization temperature before the full mesostructural collapse. The average size of nanocrystals is in the range of 7–16.5 nm, which decreases with the decline of Ti/Si ratio. Both the size and crystallinity of nanocrystals increase with the temperature elevation. The mesopore channels are large, ordered and uniform. The mean pore size is in the range of 4.3–7.4 nm, which overall decreases with the rises of Ti/Si ratio and temperature. The BET specific surface areas of the composites before the complete collapse of mesostructures are high ( $>70 \text{ m}^2 \text{ g}^{-1}$ ). The band gaps slightly increases with the decrease of Ti/Si ratio and decreases with the temperature rise. The adsorption of RhB is overwhelmingly driven by the Si-OH groups. The photocatalytic degradation activities enhance with the increase of the size and crystallinity of nanocrystals under maintaining the mesostructural integrity, and the decrease of

band gaps. There are no correlations between the activities and BET surface areas, and between the activities and acidic properties on our composites investigated. The percentage of COD removal increases obviously with the decrease of initial concentration of RhB. The RhB dye was not only decolorized but degraded as well. Our results show that the synergetic roles of coupled adsorption and photocatalytic oxidation remarkably enhance the activities, but the synchronous role generates excellent degradation activity of RhB ( $k = 0.231 \text{ min}^{-1}$ ), which is much higher than that of commercial P25 photocatalyst ( $k = 0.0671 \text{ min}^{-1}$ ).

## Supplementary materials

Other related preparation methods, characterization, figure for the change of specific surface area with crystallizing temperature, SAXRD and WAXRD patterns,  $\text{N}_2$  adsorption-desorption isotherms and pore size distributions, performances of adsorption and photocatalytic oxidation of RhB.

## Acknowledgments

This work was supported by the Start-up Research Fund for Returning Scholars from the Education Ministry of China (KEH1829028). W.Y. Dong thanks Korean Federation of Science and Technology Societies for an International Visiting Scholar supported through Brain-Pool Program. We thank Dr. S.H. Xie, associate Prof. Z.F. Lei for characterization assistance.

## Appendix A. Supplementary data

Supplementary data associated with this article can be found, in the online version, at doi:10.1016/j.apcatb.2009.12.025.

## References

- [1] H. Kyung, J. Lee, W. Choi, *Environ. Sci. Technol.* 39 (2005) 2376–2382.
- [2] X. Li, J. Ye, *J. Phys. Chem. C* 111 (2007) 13109–13116.
- [3] C. Bauer, P. Jacques, A. Kalt, *J. Photochem. Photobiol. A: Chem.* 140 (2001) 87–92.
- [4] J.C. Garcia, J.L. Oliveira, A.E.C. Silva, C.C. Oliveira, J. Nozaki, N.E. De Souza, *J. Hazard. Mater.* 147 (2007) 105–110.
- [5] Y. Xu, Y. He, X. Cao, D. Zhong, J. Jia, *Environ. Sci. Technol.* 42 (2008) 2612–2617.
- [6] Z. Chen, D. Li, W. Zhang, Y. Shao, T. Chen, M. Sun, X. Fu, *J. Phys. Chem. C* 113 (2009) 4433–4440.
- [7] K. Kadirvelu, C. Karthika, N. Vennilamani, S. Patabhi, *Chemosphere* 60 (2005) 1009–1017.
- [8] R. Jain, M. Mathur, S. Sikarwar, A. Mittal, *J. Environ. Manag.* 85 (2007) 956–964.
- [9] S. Zhu, T. Xu, H. Fu, J. Zhao, Y. Zhu, *Environ. Sci. Technol.* 41 (2007) 6234–6239.
- [10] H.-L. Chiang, K.-H. Lin, S.-Y. Chen, C.-G. Choa, S.-D. Pan, *Dyes Pigment* 75 (2007) 52–59.
- [11] D.S. Kim, Y.S. Park, *Chem. Eng. J.* 139 (2008) 256–263.
- [12] J.-M. Wu, *Environ. Sci. Technol.* 41 (2007) 1723–1728.
- [13] I.A.W. Tan, A.L. Ahmad, B.H. Hameed, *J. Hazard. Mater.* 154 (2008) 337–346.
- [14] C. Anderson, A.J. Bard, *J. Phys. Chem.* 99 (1995) 9882–9885.
- [15] T. Peng, D. Zhao, K. Dai, W. Shi, K. Hirao, *J. Phys. Chem. B* 109 (2005) 4947–4952.

- [16] J. Zhao, T. Wu, K. Wu, K. Oikawa, H. Hidaka, N. Serpone, *Environ. Sci. Technol.* 32 (1998) 2394–2400.
- [17] D. Zhao, C. Chen, Y. Wang, W. Ma, J. Zhao, T. Rajh, L. Zang, *Environ. Sci. Technol.* 42 (2008) 308–314.
- [18] Q. Wang, C. Chen, D. Zhao, W. Ma, J. Zhao, *Langmuir* 24 (2008) 7338–7345.
- [19] R. Liu, Y. Ren, Y. Shi, F. Zhang, L. Zhang, B. Tu, D.Y. Zhao, *Chem. Mater.* 20 (2008) 1140–1146.
- [20] H. Fu, S. Zhang, T. Xu, Y. Zhu, J. Chen, *Environ. Sci. Technol.* 42 (2008) 2085–2091.
- [21] S. Horikoshi, A. Saitou, H. Hidaka, N. Serpone, *Environ. Sci. Technol.* 37 (2003) 5813–5822.
- [22] F. Herrera, J. Kiwi, A. Lopez, V. Nadtochenko, *Environ. Sci. Technol.* 33 (1999) 3145–3151.
- [23] X. Chen, S.S. Mao, *Chem. Rev.* 107 (2007) 2891–2959.
- [24] A. Haarstrick, O.M. Kut, E. Heinzle, *Environ. Sci. Technol.* 30 (1996) 817–824.
- [25] Y. Xu, C.H. Langford, *J. Phys. Chem.* 99 (1995) 11501–11507.
- [26] C. Anderson, A.J. Bard, *J. Phys. Chem. B* 101 (1997) 2611–2616.
- [27] T. Torimoto, S. Ito, S. Kuwabata, H. Yoneyama, *Environ. Sci. Technol.* 30 (1996) 1275–1281.
- [28] M. Takeuchi, T. Kimura, M. Hidaka, D. Rakhmawaty, M. Anpo, *J. Catal.* 246 (2007) 235–240.
- [29] Y. Shiraishi, N. Saito, T. Hirai, *J. Am. Chem. Soc.* 127 (2005) 12820–12822.
- [30] Y. Xu, C.H. Langford, *J. Phys. Chem. B* 101 (1997) 3115–3121.
- [31] W. Wang, M. Song, *Micropor. Mesopor. Mater.* 96 (2006) 255–261.
- [32] H. Tada, Y. Kubo, M. Akazawa, S. Ito, *Langmuir* 14 (1998) 2936–2939.
- [33] H. Tada, M. Yamamoto, S. Ito, *Langmuir* 15 (1999) 3699–3702.
- [34] N. Bao, X. Feng, Z. Yang, L. Shen, X. Lu, *Environ. Sci. Technol.* 38 (2004) 2729–2736.
- [35] W.Y. Dong, Y.J. Sun, C.W. Lee, W.M. Hua, X.C. Lu, Y.F. Shi, S.C. Zhang, J.M. Chen, D.Y. Zhao, *J. Am. Chem. Soc.* 129 (2007) 13894–13904.
- [36] Ministry of Environmental Protection of People's Republic of China, *Standard Methods for the Determination of Water and Wastewater*, 4th ed., China Environmental Science Press, Beijing, 2002, pp. 211–213 (in Chinese).
- [37] S. Haukka, E.L. Lakomaa, A. Root, *J. Phys. Chem.* 97 (1993) 5085–5094.
- [38] X. Gao, I.E. Wachs, *Catal. Today* 51 (1999) 233–254.
- [39] K. Hadjiivanov, B.M. Reddy, H. Knözinger, *Appl. Catal. A* 188 (1999) 355–360.
- [40] N.N. Trukhan, A.A. Panchenko, E. Roduner, M.S. Mel'gunov, O.A. Kholdeeva, J. Mrowiec-Białoń, A.B. Jarzȳbski, *Langmuir* 21 (2005) 10545–10554.
- [41] X. Wang, J. Yu, Y. Hou, X. Fu, *Adv. Mater.* 17 (2005) 99–102.
- [42] X. Wang, J. Yu, P. Liu, X. Wang, W. Su, X. Fu, *J. Photochem. Photobiol. A* 179 (2006) 339–347.
- [43] M.A. Butler, *J. Appl. Phys.* 48 (1977) 1914–1920.
- [44] L. Peng, L. Xu, J. Yin, *Acta Phys. Sin.* 56 (2007) 1585–1589.
- [45] M. Galán-Fereres, L.J. Alemany, R. Mariscal, M.A. Bañares, J.A. Anderson, J.L.G. Fierro, *Chem. Mater.* 7 (1995) 1342–1348.
- [46] Y.-Z. Li, S.-J. Kim, *J. Phys. Chem. B* 109 (2005) 12309–12315.
- [47] A.B. Murphy, *Sol. Energy Mater. Sol. Cells* 91 (2007) 1326–1337.